JGR Space Physics

Multi-Parameter Chorus and Plasmaspheric Hiss Wave Models

Homayon Aryan[1] , **Jacob Bortnik[1]** , **Nigel P. Meredith[2]** , **Richard B. Horne[2]** , **David G. Sibeck[3]** , and **Michael A. Balikhin[4]**

[1]Atmospheric and Oceanic Sciences, University of California Los Angeles, Los Angeles, CA, USA, [2]British Antarctic Survey, Cambridge, UK, [3]NASA Goddard Space Flight Center, Greenbelt, MD, USA, [4]Department of Automatic Control and Systems Engineering, University of Sheffield, Sheffield, UK

Abstract The resonant interaction of energetic particles with plasma waves, such as chorus and plasmaspheric hiss waves, plays a direct and crucial role in the acceleration and loss of radiation belt electrons that ultimately affect the dynamics of the radiation belts. In this study, we use the comprehensive wave data measurements made by the Electric and Magnetic Field Instrument Suite and Integrated Science instruments on board the two Van Allen probes, to develop multi-parameter statistical chorus and plasmaspheric hiss wave models. The models of chorus and plasmaspheric hiss waves are presented as a function of combined geomagnetic activity (AE), solar wind velocity (V), and southward interplanetary magnetic field (Bs). The relatively smooth wave models reveal new features. Despite, the coupling between geomagnetic and solar wind parameters, the results show that each parameter still carries a sufficient amount of unique information to more accurately constrain the chorus and plasmaspheric hiss wave intensities. The new wave models presented here highlight the importance of multi-parameter wave models, and can improve radiation belt modeling.

Plain Language Summary The Van Allen radiation belts are donut-shaped belts around the Earth that consist of highly energetic particle populations. These trapped energetic particles represent a serious hazard to the electronic components of satellite. The impact can be severe and could lead to permanent failure of individual electronic subsystems and in some cases even lead to the complete loss of the satellites. The dynamics of the radiation belts are largely dictated by wave-particle interactions with plasma waves, such as chorus and plasmaspheric hiss waves. In this study, we use comprehensive wave data from the entire Van Allen Probes mission to develop multi-parameter wave models as a function of geomagnetic activity and solar wind conditions combined. The new wave models can improve radiation belt modeling through more accurate wave specification.

1. Introduction

The Van Allen radiation belts, first discovered more than 60 years ago (Van Allen, 1959), are composed of highly energetic (MeV) particle populations mainly trapped in two distinctive donut-shaped zones separated by a lower intensity slot region (Abel & Thorne, 1998; Lyons & Thorne, 1973; Lyons et al., 1972). These energetic radiation belt electrons represent a serious hazard to satellite electronic components (Blake et al., 1992). During intense geomagnetic conditions the outer radiation belt energetic electron populations exhibit dramatic variability that can cause severe and permanent damage to individual electronic subsystems, and may even lead to complete loss of the satellite (Blake et al., 1992; Fennell et al., 2001). Despite 6 decades of ongoing research, the complete dynamics of the Van Allen radiation belts is not comprehensively understood yet. It remains, both scientifically and practically crucial to understand the dynamics of the Van Allen radiation belts and thus improve space weather predictions. Hence, the Van Allen radiation belts have been the subject of many scientific studies. It is very important to understand this environment and how it is affected by geomagnetic and solar wind variability. Generally, the Van Allen radiation belt dynamics arise from a delicate balance between acceleration, transport, and loss of electrons (Baker et al., 2014; Chen et al., 2007; Foster et al., 2014; Kanekal et al., 2015; Reeves et al., 2003, 2013). The interaction of gyroresonant wave particles with plasma waves play a direct and crucial role in the acceleration and loss of radiation belt electrons that ultimately affect the dynamics of the radiation belts (Bortnik & Thorne, 2007; Horne et al., 2005; W. Li et al., 2009, 2011, 2014; Meredith et al., 2003, 2012; Thorne, 2010;

Thorne et al., 2013; Xiao et al., 2010). The most conspicuous are very low frequency (VLF) waves, such as chorus and plasmaspheric hiss, that largely dictate the dynamics of the radiation belts. Chorus and plasmaspheric hiss waves are observed in different regions of the inner magnetosphere. Chorus waves are confined in the lower-density region outside the plasmasphere, whereas plasmaspheric hiss waves are confined in the higher-density region inside the plasmasphere.

Substorms and periods of enhanced convection produce seed electron populations, with energies of tens to hundreds of keV, that are transported into geosynchronous orbit (Boyd et al., 2014; X. F. Li & Cho, 1997; Meredith et al., 2003; Obara et al., 2000; Tu et al., 2014), forming an important source for the energetic electrons in the radiation belts. The seed electrons are further energized to highly relativistic energies (>1 MeV), over broad regions of the outer radiation belt on timescales of hours (Agapitov et al., 2019; Baker & Kanekal, 2008; Baker et al., 2014; Foster et al., 2014; Horne & Thorne, 2003; Jaynes et al., 2015; Meredith et al., 2003; Reeves et al., 2013; Summers et al., 1998) through local acceleration by wave particle interactions (Baker & Kanekal, 2008; Horne & Thorne, 1998, 2003; Horne et al., 2005; Summers et al., 2002; Thorne, 2010; Thorne et al., 2005).

Chorus emissions are observed in the frequency range of $0.1f_{ce} < f < f_{ce}$, with the lower band of chorus occupying $0.1f_{ce} < f < 0.5f_{ce}$ and the upper band chorus extending over $0.5f_{ce} < f < f_{ce}$), as short coherent pulses (Burtis & Helliwell, 1969; Tsurutani & Smith, 1974), where f_{ce} is the local electron gyrofrequency. They are understood to be very intense right hand polarized electromagnetic whistler mode waves excited by the injection of substorm electrons in the vicinity of the geomagnetic equator (Burtis & Helliwell, 1969; Lauben et al., 2002; LeDocq et al., 1998; Meredith et al., 2001, 2003; Tsurutani & Smith, 1974) associated with the electron temperature anisotropy plasma instability (Kennel & Petschek, 1966). Chorus waves make significant contributions to the production of the diffuse aurora (Ni et al., 2008; Thorne, 2010). It is believed that the lower band chorus is the dominant scattering process leading to pulsating auroral precipitation (Nishimura et al., 2010, 2011) and an important source of plasmaspheric hiss waves (Agapitov et al., 2018; Bortnik et al., 2008, 2009, 2016; Meredith et al., 2013).

Plasmaspheric hiss is typically observed in the frequency range 100 Hz $< f <$ 2 kHz with a lower power than chorus (Meredith et al., 2004). Plasmaspheric hiss waves are right hand polarized electromagnetic whistler mode wave (Bortnik et al., 2008, 2009; Thorne et al., 1973) observed as a steady, incoherent noise band (Falkowski et al., 2017; Tsurutani et al., 2015, 2018). They are excited naturally in the high plasma density region inside the plasmasphere and dayside plasmaspheric plumes (Chan & Holzer, 1976; Hayakawa et al., 1986; Parrot & Lefeuvre, 1986). Plasmaspheric hiss waves are largely responsible for the continuous scattering of radiation belt electrons into the atmospheric loss cone, the decay of energetic electrons in the outer radiation belt during relatively quiet geomagnetic conditions (Lyons et al., 1972; Meredith et al., 2006; Summers et al., 2007) due to resonant pitch angle scattering of energetic electrons (Lyons et al., 1972), and are responsible for the formation of the slot region (Abel & Thorne, 1998; Lyons & Thorne, 1973; Lyons et al., 1972).

Chorus and plasmaspheric hiss emissions depend on geomagnetic activity (Agapitov et al., 2013; Aryan et al., 2014, 2016, 2017; W. Li et al., 2009, 2013; Meredith et al., 2012, 2018, 2020) and solar wind parameters (Aryan et al., 2014, 2016, 2017). The average intensities of these waves are generally statistically modeled as a function of spatial location (L-shell [L], magnetic local time [MLT], and magnetic latitude[MLat]), solar wind parameters (solar wind velocity [V], solar wind density [n], and southward interplanetary magnetic field [Bs]) (Aryan et al., 2014, 2016), geomagnetic activity as expressed by the geomagnetic indices (AE, Kp, or Dst) (Agapitov et al., 2013; Aryan et al., 2014, 2016; W. Li et al., 2009; Meredith et al., 2012), and even as a function of combined solar wind parameter and geomagnetic indices (Aryan et al., 2016). These statistical wave models are needed to calculate diffusion coefficients in radiation belt models, such as the Comprehensive Inner Magnetosphere-Ionosphere (CIMI) model (Aryan et al., 2017; Fok et al., 2008, 2011, 2014), the Versatile Electron Radiation Belt (VERB) code (Shprits et al., 2009; Subbotin & Shprits, 2009), and British Antarctic Survey (BAS) Radiation Belt Model (BAS-RBM) (Glauert et al., 2014).

Aryan et al. (2017) used the CIMI model to demonstrate that combined parameter (combination of a solar wind parameter with the AE index) wave models perform better than single parameter wave models in

radiation belt modeling. They concluded that the results could improve further with a more sophisticated combination of parameters using a larger wave database. In this study we develop multi-parameter chorus and plasmaspheric hiss wave models as a function of all three most influential geomagnetic activity (AE) and solar wind (V and Bs) parameters combined (Aryan et al., 2014, 2016; Boynton et al., 2018). The magnetosphere is a complex system so it is necessary to include all the most influential parameters that affects the wave emissions. Multi-parameter wave models are very important to achieve a more realistic representation of wave distributions in the inner magnetosphere. However, multi-parameter statistical wave models require vast data sets that poses a challenge. The current study was made possible, thanks to the comprehensive wave data measurements by the Electric and Magnetic Field Instrument Suite and Integrated Science (EMFISIS) instruments on board the two Van Allen probes. The new wave models can be used in radiation belt models, such as the CIMI model, the VERB code, and the BAS-RBM, to improve radiation belt modeling.

2. Data

The twin NASA Van Allen probes were launched on August 30, 2012 to understand the processes responsible for causing variability of the Van Allen radiation belts. The mission ended in 2019 after collecting almost 7 years of valuable data. The two identical probes (Probe A and B) were launched into highly elliptical (a perigee of ~1.1 Re and an apogee of ~5.8 Re geocentric) and low inclination orbits (inclination of ~10°) (Mauk et al., 2013). This allowed the Van Allen Probes to spend prolonged periods of time in the most critical regions of the radiation belts and collect comprehensive wave data. The two probes orbited the Earth every ~9 h which enabled the satellites to traverse the radiation belts approximately five times per day. Probes A and B completed more than three full precessions about all MLTs before they were decommissioned in October 2019 and July 2019, respectively. The EMFISIS instruments on board the Van Allen Probes were designed specifically to observe plasma waves in the inner magnetosphere. The EMFISIS suite included a waveform receiver (WFR) (Kletzing et al., 2013; Wygant et al., 2013) that measured wave power spectral density in the range 10 Hz < f < 12 kHz with full 3-D spectral matrix every 6 s along with a selection of burst modes that provided full waveforms with a sampling rate of approximately 35 kHz (Kletzing et al., 2013). Each EMFISIS suite also carried a high-frequency receiver (HFR) instrument that measured electric spectral intensity between 10 and ~400 kHz. The triaxial fluxgate and triaxial search coil magnetometers measured the background magnetic fields and high frequency wave magnetic field fluctuations respectively that are used to calculate wave polarization properties (Santolík & Gurnett, 2003).

We use the comprehensive wave data measurements from the EMFISIS instruments, for the entire Van Allen Probes mission, to develop multi-parameter statistical chorus and plasmaspheric hiss wave models. The magnetic field intensities, Bw, for chorus waves are calculated by integrating the wave spectral intensities (pT^2 Hz^{-1}) over the frequency range $0.1f_{ce} < f < 0.5f_{ce}$ (Aryan et al., 2014, 2016; Meredith et al., 2001, 2012). On the other hand, for plasmaspheric hiss, the magnetic field intensities, Bw, are calculated by integrating the wave spectral intensities (pT^2 Hz^{-1}) over the frequency range $100\ Hz < f < 2\ kHz$ (Aryan et al., 2016; Meredith et al, 2004, 2007, 2018; Thorne et al., 1973). We calculate the total plasma density using the upper hybrid resonance frequency measured by the HFR (Kurth et al., 2015). The plasmaspheric region is then defined as the region where the plasma density is higher than the larger value between 10 x $(6.6/L)^4$ and 50 cm^{-3} (W. Li et al., 2010). We distinguish chorus and plasmaspheric hiss waves by the plasma density where frequencies overlap (Sheeley et al., 2001) (please see Aryan et al. [2014] and Aryan et al. [2016] for more details).

NASA's GSFC online space physics data facility, OMNIWeb, is used to obtain the geomagnetic index (AE) and solar wind parameters (V and Bs) at relatively high resolutions. The OMNIWeb interface provides access to near Earth, one AU, solar wind magnetic field and plasma parameters data from WIND and Advanced Composition Explorer (ACE) missions at high resolution ranging between 1-min and 5-min. The database is freely available to the scientific community. For solar wind parameters we apply appropriate time delays (the maximum value of the velocity in the last 24 h and Bs from 90 min prior using the 5 min averaged data) and we use the high resolutions (1 min) instantaneous value of the AE index (Aryan et al., 2014, 2016, 2017).

3. Results and Discussions

The intensities of chorus and plasmaspheric hiss waves are often mapped, statistically, in L, MLT, and MLat as a function of geomagnetic activity (Agapitov et al., 2013; Aryan et al., 2014, 2016, 2017; W. Li et al., 2009; Meredith et al., 2012;) or solar wind parameters (Aryan et al., 2014, 2016, 2017). Here, we bin the intensities of these waves in L and MLT as a function of all three most influential geomagnetic activity (AE) and solar wind (V and Bs) parameters combined (Aryan et al., 2014, 2016; Boynton et al., 2018). Such multi-parameter wave models require a vast dataset, which we now have available in the form of almost 7 years of EMFISIS wave measurements on board the two Van Allen Probes.

The chorus and plasmaspheric hiss wave intensities are separately binned in linear steps of 0.1 L (from $L = 2.8$ to ~ 6.5 L) and 1 h MLT as a function of AE, V, and Bs. The geomagnetic activity, as represented by the geomagnetic AE index, is split into three intervals: quiet when AE < 100 nT; moderate when $100 \leq$ AE ≤ 300 nT; and active when AE > 300 nT. The solar wind velocity, V, is split into three intervals: slow when $V < 400$ km/s; moderate when $400 \leq V \leq 600$ km/s; and fast when $V > 600$ km/s. Finally, the Bs is also split into three intervals: low when Bs < 4 nT; moderate when $4 \leq$ Bs ≤ 8 nT; and high when Bs > 8 nT. This leads to 27 different combinations of wave intensities in L and MLT, for each wave type. We then perform averaging to make sure the wave models have relatively smooth wave intensity variation in L and MLT. Generally, these statistical wave models show sporadic variation in wave intensities, especially, for bins representing extreme conditions where there are relatively fewer number of cases (for example, Figure 1 of Aryan et al. [2016] and also similar figures in Meredith et al. [2012], Agapitov et al. [2013], and Aryan et al. [2017]). However, it is important to have more gradually varying wave intensities along L and MLT, when incorporating these models into radiation belt models such as the CIMI model (Aryan et al., 2017; Fok et al., 2008, 2011, 2014). Hence, in this study we apply a moving average technique along L and MLT respectively. The moving average along the L-shell takes into account the wave intensities of the current bin and its two neighboring bins on each side (for example; for the bin $4.0 \leq L < 4.1$ the moving average takes into account the intensity of $3.8 \leq L < 3.9$, $3.9 \leq L < 4.0$, $4.0 \leq L < 4.1$, $4.1 \leq L < 4.2$, and $4.2 \leq L < 4.3$ bins) due to the small bin sizes (0.1 L) and expected small variations in wave intensities across small steps of L-shell. The moving average along MLT, however, takes into account the wave intensity of the current bin and only one neighboring bin on each side (for example, for the bin $7 \leq$ MLT < 8, the moving average takes into account the intensity of $6 \leq$ MLT < 7, $7 \leq$ MLT < 8, and $8 \leq$ MLT < 9 bins) due to relatively larger variation in wave intensities across each MLT (1 h MLT) bin. The smoothing technique (number of neighboring bins to smooth) was carefully chosen to provide smooth wave models while preserving wave intensities; smoothing over too many bins could result in losing information, however, smoothing over too few bins may not provide smooth wave intensity distributions.

Figure 1 shows the average chorus wave intensities observed by the Van Allen Probes as a function of L, MLT, AE, V and Bs. From left to right, the panels show increasing AE (low AE [a, d, g, j, m, p, s, v, y], moderate AE [b, e, h, k, n, q, t, w, z], and high AE [c, f, i, l, o, r, u, x, zz]). The solar wind velocity increases down the rows of the panels and repeats after every three rows (slow V [a, b, c, j, k, l, s, t, u], moderate V [d, e, f, m, n, o, v, w, x], fast V [g, h, i, p, q, r, y, z, zz]). From top to bottom, Bs increases in groups of three panels (low Bs [a–i], moderate Bs [j–r], high Bs [s–zz]). The results show that generally chorus wave intensities increase with increasing geomagnetic activity, solar wind velocity and southward interplanetary magnetic field. The most intense wave emissions are observed during active conditions (high AE, fast V, and high Bs) from around midnight to midday. The lowest wave intensities, however, are observed during quiet times (low AE, slow V and low Bs) consistent with past studies (Agapitov et al., 2013; Aryan et al., 2014, 2016, 2017; W. Li et al., 2009; Meredith et al., 2012). It is clear that all three geomagnetic and solar wind parameters (AE, V, and Bs) are important in defining the intensity of chorus wave emissions. Even though these parameters are known to be coupled (McPherron et al., 2015), it is clear from the forgoing analysis that each parameter still carries a sufficient amount of unique information to more accurately constrain the chorus intensities. To understand this better, we look at the importance of each parameter individually. For example, considering the middle row (panels m, n, and o), the chorus wave intensities increase as geomagnetic activity increases (lowest wave intensities are observed in panel m for low AE, but the highest wave intensities are observed in panel o for high AE), while V and Bs are moderate and remain unchanged. Similarly, considering panels l, o and r where AE and Bs remain high and moderate respectively, the chorus wave intensities increase with
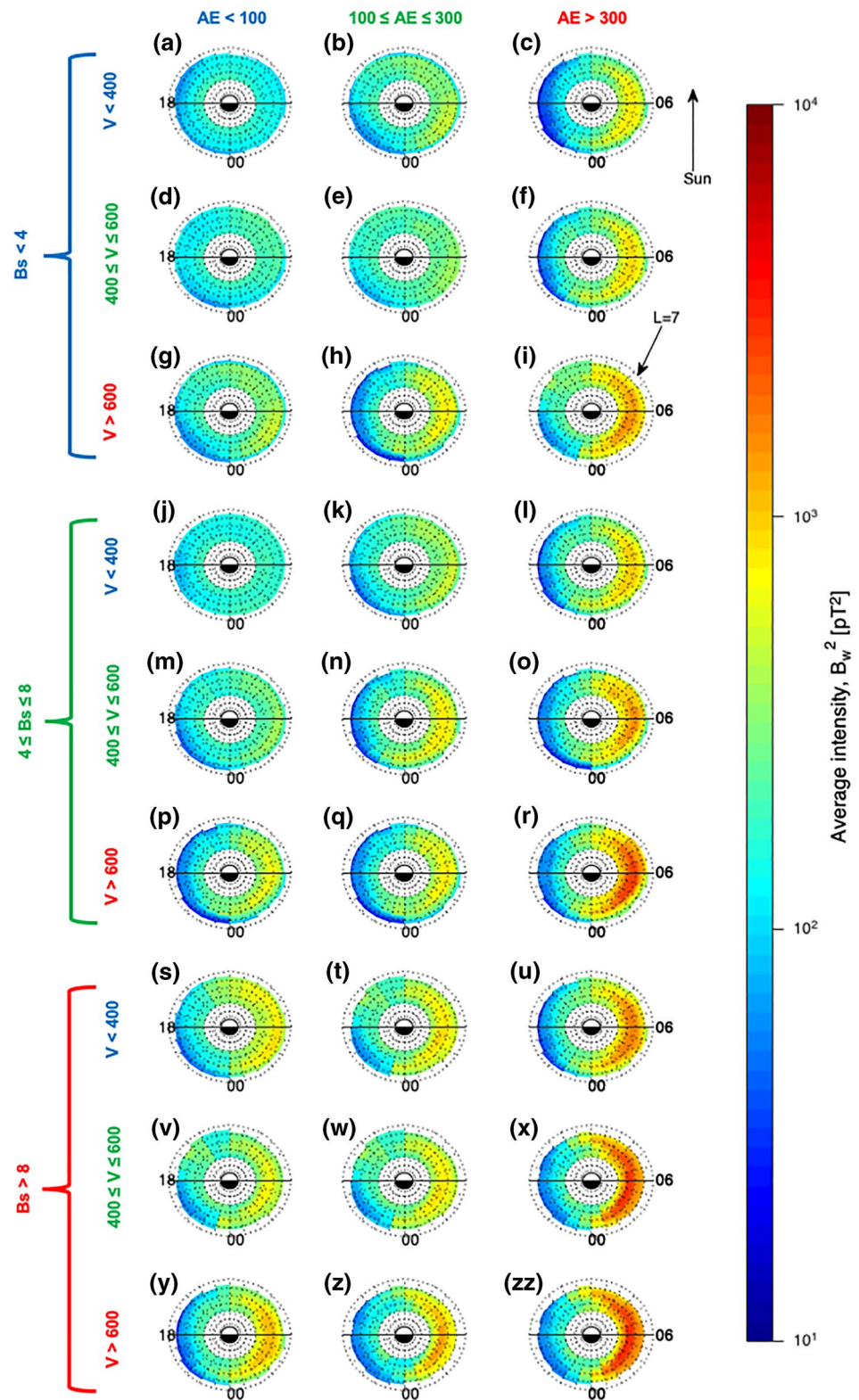
Figure 1. The average chorus wave intensities observed by the Van Allen Probes as a function of L, MLT, AE, V and Bs. From left to right the panels show increase in AE (low AE [a, d, g, j, m, p, s, v, y], moderate AE [b, e, h, k, n, q, t, w, z], and high AE [c, f, i, l, o, r, u, x, zz]). The solar wind velocity increases down the panels and repeats after every three panels (slow V [a, b, c, j, k, l, s, t, u], moderate V [d, e, f, m, n, o, v, w, x], fast V [g, h, i, p, q, r, y, z, zz]). From top to bottom, Bs increases in groups of three panels (low Bs [a–i], moderate Bs [j–r], and high Bs [s–zz]).
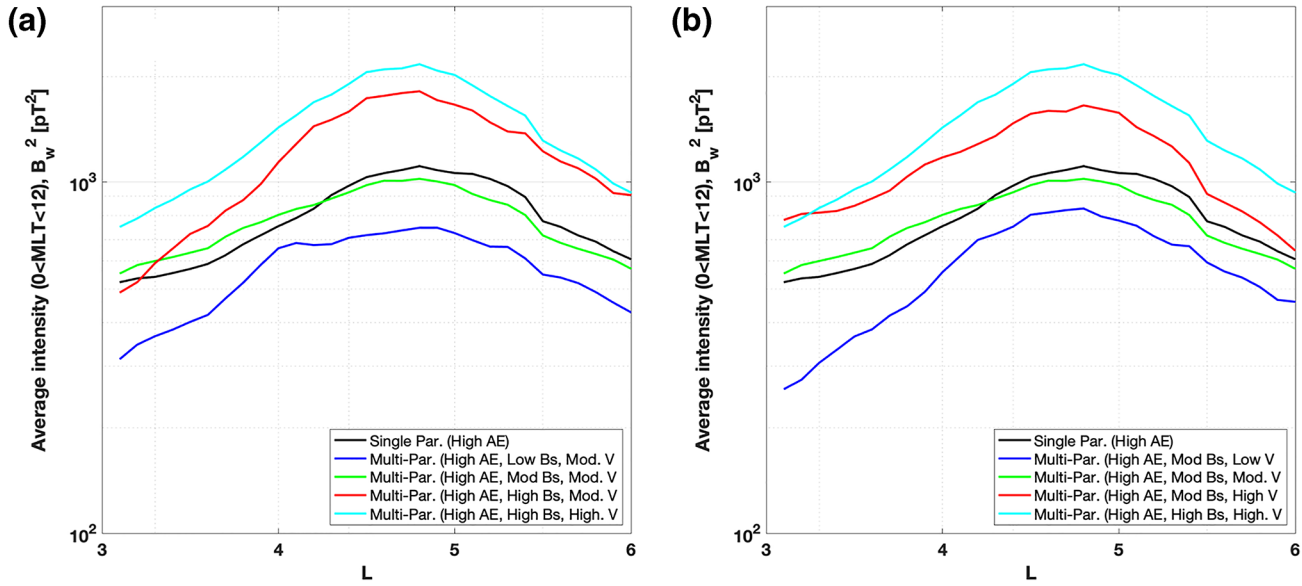
Figure 2. The average chorus wave intensities for a single parameter AE wave model, for high AE, compared with multi-parameter wave models for high AE but various different Bs and V conditions. The x-axis is the L-shell and the y-axis is the average chorus wave intensity for MLT between mid-night to mid-day (where chorus is more prominent). The black lines show the average chorus wave intensity for a single parameter AE wave model for high AE. The red, green, blue and light blue lines represent multi-parameter wave models for high AE but different Bs and V conditions. In both panels (a and b), the light blue lines represents extreme conditions (high AE, high Bs, and fast V). In panel a, for the red, green and blue lines, the Bs is the only changing variable (high Bs [red line], moderate Bs [green line], and low Bs [blue line]), the AE and V are high and moderate respectively and remain unchanged. However, in panel b, for the red, green and blue lines, the solar wind velocity is the only changing parameter (fast V [red line], moderate V [green line], and slow V [blue line]), the AE and Bs are high and moderate respectively and remain unchanged.

solar wind velocity (lowest wave intensities are observed in panel l for slow V, but the highest wave intensities are observed in panel r for fast V). Finally, in panels i, r, and zz, the Bs is the only changing parameter, it is clear that the chorus wave intensities increase as Bs turns more southward (lowest wave intensities are observed in panel i for low Bs, but the highest wave intensities are observed in panel zz for high Bs). In the later case, the AE and V are both high in all three panels (i, r, and zz), however, the peak wave intensities for low Bs is up to a magnitude lower than the peak wave intensities for high Bs (as in panel i compared to panel zz). This emphasizes the importance of each parameter in multi-parameter wave models. Estimating wave intensities using a single parameter wave model may not be accurate. For example, in a single parameter wave model, such as a chorus wave model based on the AE index alone, the peak wave intensities for low AE (<100) conditions would be expected to be ~10^2 [pT^2] (Aryan et al., 2014, 2016). However, as shown in panel y, the peak wave intensities can be an order of a magnitude higher (~10^3 [pT^2]), providing that the solar wind velocity is fast and the Bs is highly southwards. In addition, it is worth noting that the general understating is that chorus wave activity increases everywhere as Bz turns southward, solar wind velocity increases, and AE increases. But the results presented in Figure 1 shows that this may not always necessary be the case. At some MLTs the chorus wave activity may actually decrease as AE, V, and Bs increases. For example, the AE index increases from panels a to c, while V and Bs remains unchanged, but the chorus wave intensities for some MLTs on the dusk side decreases. This could be due to strong Landau damping by suprathermal electrons (Bortnik & Thorne, 2007).

The difference between single and multi-parameter wave models can be determined by directly comparing the wave intensities from a single parameter wave model with multi-parameter wave models presented in current study. Figure 2 shows the average chorus wave intensities for a single parameter AE wave model, for high AE, compared with multi-parameter wave models for high AE but various different Bs and V conditions. The x-axis is the L-shell and the y-axis is the average chorus wave intensity for MLT between midnight to mid-day (where chorus is more prominent). The black lines show the average chorus wave intensity for a single parameter AE wave model for high AE. The red, green, blue and light blue lines represent multi-parameter wave models for high AE but different Bs and V conditions. In both panels, the light blue lines
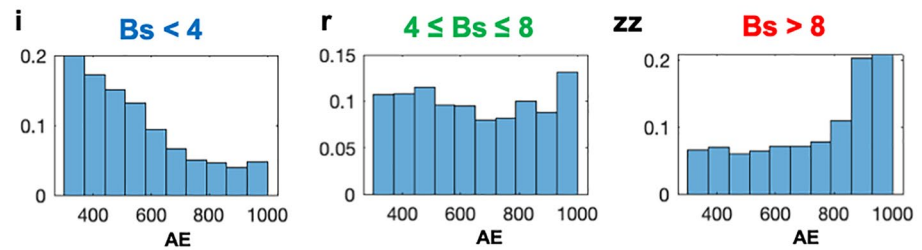
Figure 3. The distribution of AE index in panels i, r, and zz of Figure 1.

represent extreme conditions (high AE, high Bs and fast V). In panel a, for the red, green and blue lines, the Bs is the only changing variable (high Bs [red line], moderate Bs [green line], and low Bs [blue line]), the AE and V are high and moderate respectively and remain unchanged. On the other hand, in panel b, for the red, green and blue lines, the solar wind velocity is the only changing parameter (fast V [red line], moderate V [green line], and slow V [blue line]), the AE and Bs are high and moderate respectively and remain unchanged. It's clear that, when the Bs and V are moderate, the wave intensity is roughly similar for single parameter (black lines) and multi-parameter (green lines) wave models. However, as we can see in panel a, when Bs is high (red line), the single parameter wave model underestimates the wave intensities and vice versa. Also the same effect can be observed in panel b for changing solar wind velocity. In this case, when V is high (red line), the single parameter wave model under estimates the wave intensities and vice versa. The difference between wave intensities for single parameter (black line) and multi-parameter wave models is more significant during extreme conditions (light blue line).

The importance of multi-parameter wave models can also be shown, from a different perspective, by studying the distribution of the data binned in each panel. For example, Figure 3 shows the distribution of AE in panels i, r, and zz of Figure 1. The only parameter that is, changing in these three panels (i, r, and zz) is the Bs, the AE and V are both high in all three panels (AE > 300 nT and V > 600 km/s respectively) and remain unchanged. When Bs is low (panel i), the majority of the data binned in this panel are concentrated around lower AE values (AE = 300 to ~600 nT). However, for high Bs (panel zz), the majority of the data binned in panel zz are concentrated toward higher AE values (AE > ~700 nT). For moderate Bs (panel r) conditions, the data binned in panel r poses a more even distribution with respect to high AE. This shows that different parameters define where the data is binned. In addition, Figure 3 indicates that the wave models may improve further if the AE, V and Bs parameters are split into smaller intervals. However, splitting these parameters into smaller bins will require an even more extensive dataset, consisting of data from multiple satellite missions combined, to form meaningful statistics for wave intensities. Though, for the sake of the current study, we split the AE (for high AE values as presented in Figure 3) into smaller bins and check whether a similar pattern in the distribution of AE (as observed in Figure 3) can be observed.

Figure 4 shows the distribution of AE index for low (top row), moderate (middle row), and high (bottom row) Bs, as presented in Figure 3 but with smaller AE bins (left: 300 ≤ AE ≤ 450 nT, middle: 450 ≤ AE ≤ 700 nT, and right: AE > 700 nT). Generally, for low Bs (top row) the data selected in each bin is concentrated toward the lower AE values for each bin. On the other hand, for high Bs (bottom row) the data selected in each bin is concentrated toward the higher AE values within each bin. This is consistent with the trend observed with larger AE bins shown in Figure 3. This emphasis that multi-parameter wave models are important even if we split the AE index into smaller intervals. However, it's worth noting that the affect of data resolution (averaging) may become more significant as we split the AE index into smaller bins. The wave models presented in this study uses the instantaneous high resolution (1-min averaged) AE index data. The results may look different if different resolution data is used. For example, lower resolution (1h averaged) AE index data will eliminates some of the fast variability from the 1-min AE values. This will result in some data binned in different bins and therefore the results may look slightly different.

In addition, the same analysis can be applied to plasmaspheric hiss wave intensities. Figure 5 shows the average plasmaspheric hiss wave intensities observed by the Van Allen Probes as a function of L, MLT, AE, V and Bs. From left to right the panels show increasing AE (low AE [a, d, g, j, m, p, s, v, y], moderate
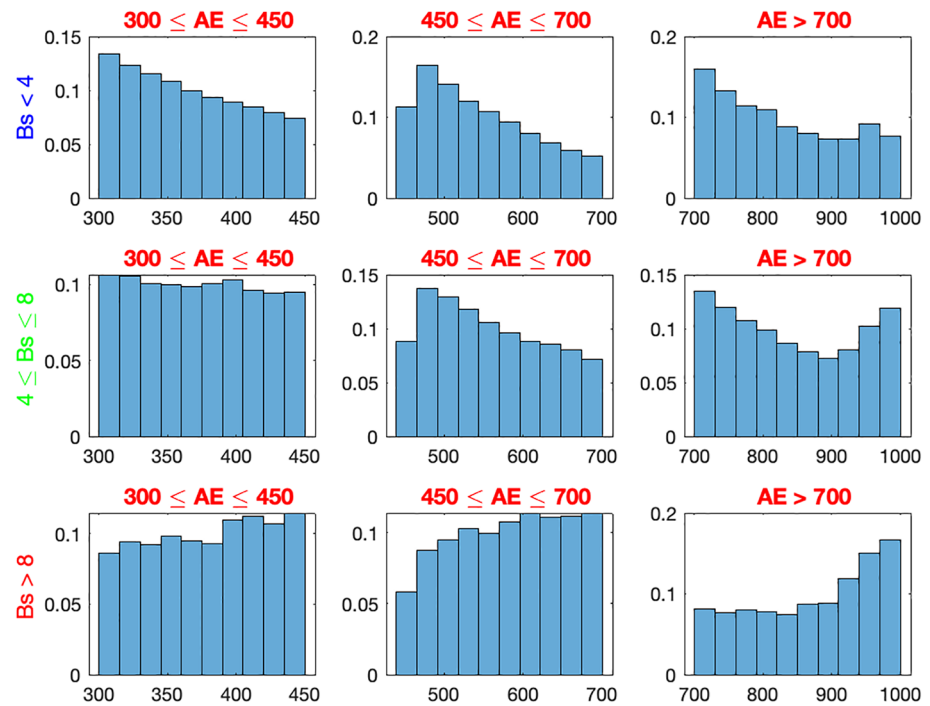
Figure 4. The distribution of AE index for low (top row), moderate (middle row), and high (bottom row) Bs, as presented in Figure 3 but with smaller AE bins.

AE [b, e, h, k, n, q, t, w, z], and high AE [c, f, i, l, o, r, u, x, zz]). The solar wind velocity increases down the panels and repeats after every three panels (for example, slow V [a, b, c, j, k, l, s, t, u], moderate V [d, e, f, m, n, o, v, w, x], fast V [g, h, i, p, q, r, y, z, zz]). From top to bottom, Bs increases in groups of three panels (for example; low Bs [a–i], moderate Bs [j–r], high Bs [s–zz]). The results show a strong day-night asymmetry with peak wave emissions primarily observed on the dayside, consistent with past studies (Aryan et al., 2017; Kim et al., 2015; W. Li et al., 2013; Malaspina et al., 2016; Meredith et al., 2004, 2007). Similar to chorus waves, the peak plasmaspheric hiss intensities increase with increasing geomagnetic activity, solar wind velocity and southward interplanetary magnetic field. The most intense wave emissions are observed during active conditions (high AE, fast V, and high Bs). The results show that all three geomagnetic and solar wind parameters (AE, V, and Bs) are important in defining the intensity of plasmaspheric hiss wave emissions. However, it should be noted that the variation of the wave intensities with respect to each parameter for plasmaspheric hiss waves is less than that observed for chorus wave emissions. For example, as we discussed above for chorus waves, the peak chorus wave intensities observed for high Bs (Figure 1[zz]) is approximately a magnitude higher than that observed for low Bs (Figure 1i) conditions. However, here in the case of plasmaspheric hiss waves, the peak wave intensities observed for high Bs (Figure 3zz) is less than a magnitude higher than that observed for low Bs (Figure 3i) conditions. This is probably due to the fact that plasmaspheric hiss waves are confined within the plasmasphere, much deeper inside the inner magnetosphere, and subsequently influenced less dramatically by the changes in AE, V, and Bs. Nevertheless, the results show that each parameter is still influential. This can be observed more clearly in Figure 6, which shows the average dayside plasmaspheric hiss wave intensities for a single parameter AE wave model, for high AE, compared with multi-parameter wave models for high AE but various different Bs and V conditions. The x-axis is the L-shell and the y-axis is the average chorus wave intensity for the dayside (where hiss is more prominent). The black lines show the average hiss wave intensity for a single parameter AE wave model for high AE. The red, green, blue, and light blue lines represent multi-parameter wave models for high AE but different Bs and V conditions. In both panels, the light blue lines represent extreme conditions (high AE, high Bs, and fast V). In panel a, for the red, green and blue lines, the Bs is the only changing variable (high Bs [red line], moderate Bs [green line], and low Bs [blue line]), the AE and V are high and moderate respectively and remain unchanged. However, in panel b, for the red, green and blue lines, the
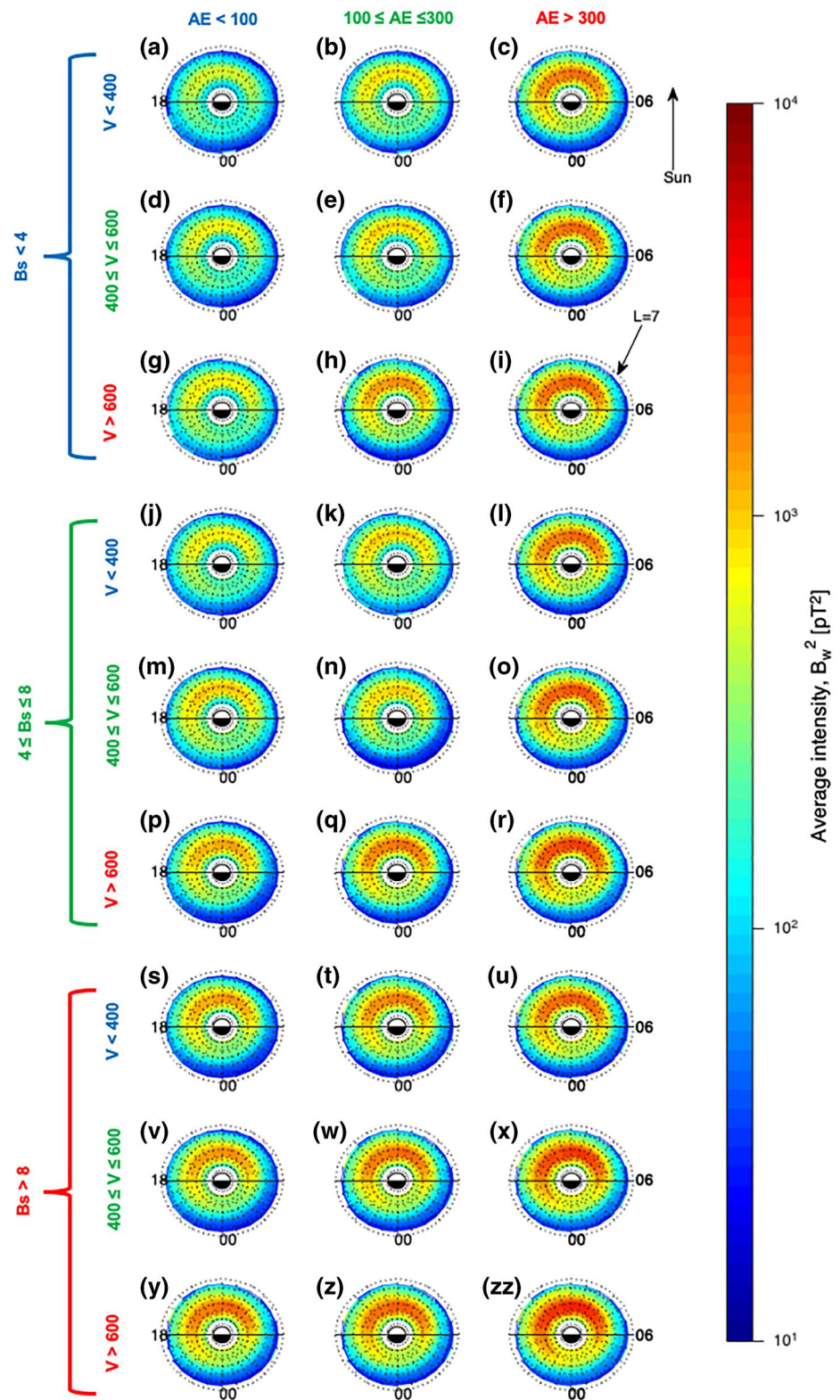
Figure 5. The average plasmaspheric hiss wave intensities observed by the Van Allen Probes as a function of L, MLT, AE, V, and Bs. Caption of Figure 1 applies.
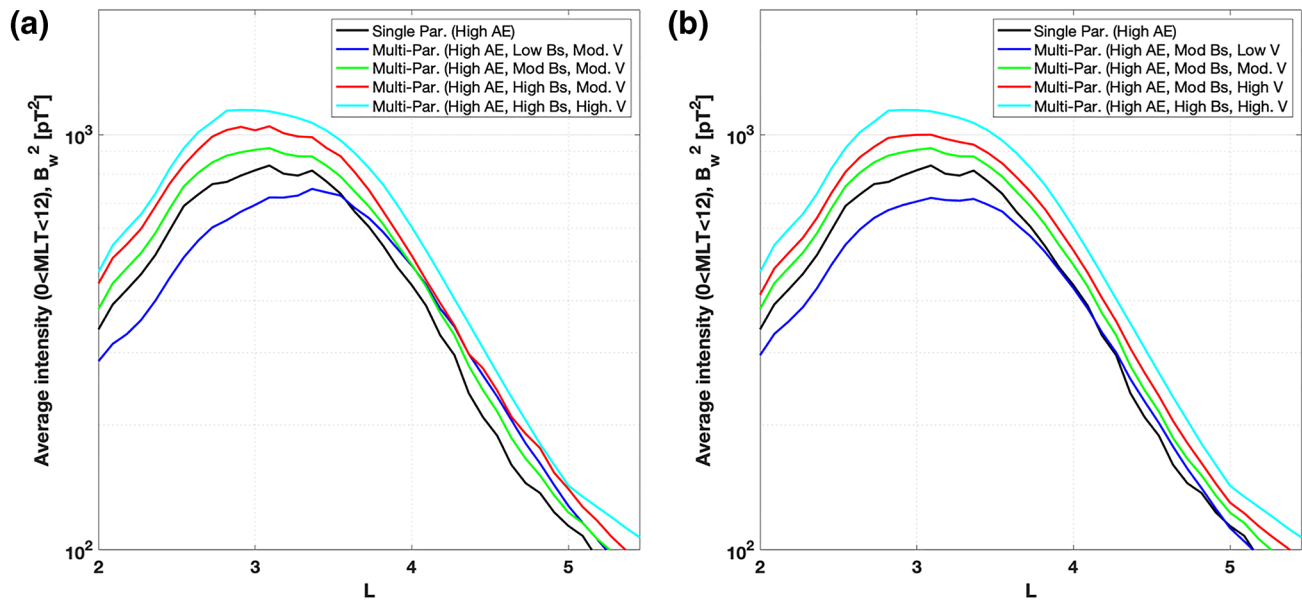
Figure 6. The average plasmaspheric hiss wave intensities for a single parameter AE wave model, for high AE, compared with multi-parameter wave models for high AE but various different Bs and V conditions. The x-axis is the L-shell and the y-axis is the average chorus wave intensity for the dayside (where hiss is more prominent). The black lines show the average hiss wave intensity for a single parameter AE wave model for high AE. The red, green, blue and light blue lines represent multi-parameter wave models for high AE but different Bs and V conditions. In both panels, the light blue lines represent extreme conditions (high AE, high Bs and fast V). In panel a, for the red, green and blue lines, the Bs is the only changing variable (high Bs [red line], moderate Bs [green line], and low Bs [blue line]), the AE and V are high and moderate respectively and remain unchanged. However, in panel b, for the red, green and blue lines, the solar wind velocity is the only changing parameter (fast V [red line], moderate V [green line], and slow V [blue line]), the AE and Bs are high and moderate respectively and remain unchanged.

solar wind velocity is the only changing parameter (fast V [red line], moderate V [green line], and slow V [blue line]), the AE and Bs are high and moderate respectively and remain unchanged. The wave intensity is roughly similar for single parameter (black lines) and multi-parameter (green lines) wave models when the Bs and V are moderate. Panel a shows that the single parameter wave model can underestimates the wave intensities when Bs is high (red line) and vice versa. Panel b shows the same effect for solar wind velocity, where a single parameter wave model can underestimates the wave intensities during fast solar wind velocities (red line) vice versa. Finally, a single parameter wave model can under estimate the wave intensities more significantly during extreme conditions (light blue line).

Overall, the wave models presented here highlights the importance of multi-parameterization. The magnetosphere is a complex system, therefore it is necessary to consider all the most influential parameters when modeling wave intensities for better accuracy. Aryan et al. (2017) demonstrated with the CIMI model that a double wave parameter model can reduce simulation error by up to 6% in compression to a single parameter wave model. We hope the new more sophisticated multi parameter wave models developed in this study, that includes all the most influential parameters (Aryan et al., 2014; Boynton et al., 2018), can provide significant improvement to radiation belt models, such as the CIMI model (Aryan et al., 2017; Fok et al., 2008, 2011, 2014), the VERB code (Shprits et al., 2009; Subbotin & Shprits, 2009) and BAS-RBM (Glauert et al., 2014), where the wave models are used for the calculation of diffusion coefficients under different geomagnetic and solar wind conditions.

4. Conclusion

In this study, we used the comprehensive wave data measurements, by the EMFISIS instrument on board the two Van Allen probes, to develop multi-parameter statistical chorus and plasmaspheric hiss wave models. The models of chorus and plasmaspheric hiss waves are presented as a function of combined geomagnetic activity (AE), solar wind velocity (V), and southward interplanetary magnetic field (Bs). This

study shows that all three most influential parameters of solar wind and geomagnetic index (AE, V and Bs) (Aryan et al., 2014) play an important role in the statistical distribution of chorus and plasmaspheric hiss wave intensities in L and MLT. Despite, the coupling between geomagnetic and solar wind parameters (McPherron et al., 2015), the results clearly show that each parameter still carries a sufficient amount of unique information to more accurately constrain the chorus and plasmaspheric hiss wave intensities. The results show that a single parameter wave model can over/under estimate the wave intensities based on the solar wind conditions. In fact, the results show that there can be significant wave activity even during low AE conditions, providing that the Bs is high and the solar wind velocity is fast.

The magnetosphere is a complex system and therefore it is necessary to consider all the most influential parameters (Aryan et al., 2014) when modeling wave intensities for better accuracy. Solar wind coupling with the magnetosphere triggers currents and electric fields, generates changes in the inner magnetosphere, and produces magnetic storms or substorms. Also, the size of the plasmasphere and the location of the plasmapause is strongly influenced by the solar wind conditions (Larsen et al., 2007). The size of the plasmasphere is reduced during higher convections due to solar wind. This allows chorus wave growth throughout broader regions of the inner magnetosphere and ultimately providing a richer source for plasmaspheric hiss waves (Agapitov et al., 2018; Bortnik et al., 2008, 2009, 2016; Meredith et al., 2013). Another advantage of the new wave models is the relatively smooth wave intensity variations in L and MLT. This can provide more convenient estimates of intensities across the whole range of L and MLTs.

The wave models could improve further if we take into account the latitude and frequency resolutions (Meredith et al., 2018, 2020), and also by splitting the AE, V, and Bs parameters into smaller intervals. However, splitting the AE, V, and Bs parameters into smaller bins or including latitude variations will require an even more extensive dataset, consisting of data from multiple satellite missions combined, to form meaningful statistics for wave intensities. Nevertheless, the results presented in this paper show that multi parameter wave models are important even if smaller intervals are used. Overall, the focus of the current study is to highlight the importance of multi parameterization. The results suggest that we can build much more sophisticated wave models in future.

The new multi parameter wave models are developed to be incorporated into radiation belt models, such as the CIMI model (Aryan et al., 2017; Fok et al., 2008, 2011, 2014), the VERB code (Shprits et al., 2009; Subbotin & Shprits, 2009) and BAS-RBM (Glauert et al., 2014), where the wave models are used to calculate the diffusion coefficients under different geomagnetic and solar wind conditions. We hope the new wave models can provide significant improvement to radiation belt models. We intend to perform such simulations and comparisons in future studies.

Data Availability Statement

The HFR and WFR data are freely available from the EMFISIS instrument (Kletzing et al., 2013; Wygant et al., 2013) website at the University of Iowa (https://emfisis.physics.uiowa.edu/). The geomagnetic index (AE) and solar wind parameters (V and Bs) are freely available from NASA's GSFC online space physics data facility, OMNIWeb (https://omniweb.gsfc.nasa.gov).

References

Abel, B., & Thorne, R. M. (1998). Electron scattering loss in Earth's inner magnetosphere 1. Dominant physical processes. *Journal of Geophysical Research*, *103*, 2385–2396. https://doi.org/10.1029/97JA02919

Agapitov, O. V., Artemyev, A., Krasnoselskikh, V., Khotyaintsev, Y. V., Mourenas, D., Breuillard, H., et al. (2013). Statistics of whistler mode waves in the outer radiation belt: Cluster STAFF-SA measurements. *Journal of Geophysical Research: Space Physics*, *118*, 3407–3420. https://doi.org/10.1002/jgra.50312

Agapitov, O. V., Mourenas, D., Artemyev, A., Hospodarsky, G., & Bonnell, J. (2019). Time scales for electron quasi-linear diffusion by lower-band chorus waves: The effects of pe/ce dependence on geomagnetic activity. *Geophysical Research Letters*, *46*(12), 6178–6187. https://doi.org/10.1029/2019GL083446

Agapitov, O. V., Mourenas, D., Artemyev, A. V., Mozer, F. S., Hospodarsky, G., Bonnell, J., et al. (2018). Synthetic empirical chorus wave model from combined Van Allen Probes and Cluster statistics. *Journal of Geophysical Research: Space Physics*, *123*(1), 297–314. https://agupubs.onlinelibrary.wiley.com/doi/abs/10.1002/2017JA024843

Aryan, H., Sibeck, D., Balikhin, M., Agapitov, O., & Kletzing, C. (2016). Observation of chorus waves by the Van Allen Probes: Dependence on solar wind parameters and scale size. *Journal of Geophysical Research: Space Physics*, *121*, 7608–7621. https://doi.org/10.1002/2016JA022775

Aryan, H., Sibeck, D. G., Kang, S.-B., Balikhin, M. A., Fok, M.-C., Agapitov, O., et al. (2017). Cimi simulations with newly developed multi-parameter chorus and plasmaspheric hiss wave models. *Journal of Geophysical Research: Space Physics*, *122*(9), 9344–9357. https://agupubs.onlinelibrary.wiley.com/doi/abs/10.1002/2017JA024159

Aryan, H., Yearby, K., Balikhin, M., Agapitov, O., Krasnoselskikh, V., & Boynton, R. (2014). Statistical study of chorus wave distributions in the inner magnetosphere using ae and solar wind parameters. *Journal of Geophysical Research: Space Physics*, *119*(8), 6131–6144. http://dx.doi.org/10.1002/2014JA019939

Baker, D. N., Jaynes, A. N., Li, X., Henderson, M. G., Kanekal, S. G., Reeves, G. D., et al. (2014). Gradual diffusion and punctuated phase space density enhancements of highly relativistic electrons: Van Allen Probes observations. *Geophysical Research Letters*, *41*(5), 1351–1358. http://dx.doi.org/10.1002/2013GL058942

Baker, D. N., & Kanekal, S. G. (2008). Solar cycle changes, geomagnetic variations, and energetic particle properties in the inner magnetosphere. *Journal of Atmospheric and Solar-Terrestrial Physics*, *70*, 195–206. https://doi.org/10.1016/j.jastp.2007.08.031

Blake, J. B., Gussenhoven, M. S., Mullen, E. G., & Fillius, R. W. (1992). Identification of an unexpected space radiation hazard. *IEEE Transactions on Nuclear Science*, *39*, 1761–1764. https://doi.org/10.1109/23.211364

Bortnik, J., Chen, L., Li, W., Thorne, R. M., Nishimura, Y., Angelopoulos, V., et al. (2016). In A. Keiling, D. H. Lee, & V. Nakariakov (Eds.), *Relationship between chorus and plasmaspheric hiss waves*. Washington, DC: American Geophysical Union Geophysical Monograph Series. https://doi.org/10.1002/9781119055006.ch6

Bortnik, J., Li, W., Thorne, R. M., Angelopoulos, V., Cully, C., Bonnell, J., et al. (2009). An observation linking the origin of plasmaspheric hiss to discrete chorus emissions. *Science*, *324*, 775. https://doi.org/10.1126/science.1171273

Bortnik, J., & Thorne, R. M. (2007). The dual role of ELF/VLF chorus waves in the acceleration and precipitation of radiation belt electrons. *Journal of Atmospheric and Solar-Terrestrial Physics*, *69*(3), 378–386. https://doi.org/10.1016/j.jastp.2006.05.030

Bortnik, J., Thorne, R. M., & Meredith, N. P. (2008). The unexpected origin of plasmaspheric hiss from discrete chorus emissions. *Nature*, *452*, 62–66. https://doi.org/10.1038/nature06741

Boyd, A. J., Spence, H. E., Claudepierre, S. G., Fennell, J. F., Blake, J. B., Baker, D. N., et al. (2014). Quantifying the radiation belt seed population in the 17 March 2013 electron acceleration event. *Geophysical Research Letters*, *41*, 2275–2281. https://doi.org/10.1002/2014GL059626

Boynton, R. J., Aryan, H., Walker, S. N., Krasnoselskikh, V., & Balikhin, M. A. (2018). The influence of solar wind and geomagnetic indices on lower band chorus emissions in the inner magnetosphere. *Journal of Geophysical Research: Space Physics*, *123*(11), 9022–9034. https://agupubs.onlinelibrary.wiley.com/doi/abs/10.1029/2018JA025704

Burtis, W. J., & Helliwell, R. A. (1969). Banded chorus - A new type of VLF radiation observed in the magnetosphere by OGO 1 and OGO 3. *Journal of Geophysical Research*, *74*, 3002. https://doi.org/10.1029/JA074i011p03002

Chan, K.-W., & Holzer, R. E. (1976). ELF hiss associated with plasma density enhancements in the outer magnetosphere. *Journal of Geophysical Research*, *81*, 2267–2274. https://doi.org/10.1029/JA081i013p02267

Chen, Y., Reeves, G. D., & Friedel, R. H. W. (2007). The energization of relativistic electrons in the outer Van Allen radiation belt. *Nature Physics*, *3*, 614–617. https://doi.org/10.1038/nphys655

Falkowski, B. J., Tsurutani, B. T., Lakhina, G. S., & Pickett, J. S. (2017). Two sources of dayside intense, quasi-coherent plasmaspheric hiss: A new mechanism for the slot region?. *Journal of Geophysical Research: Space Physics*, *122*(2), 1643–1657. https://agupubs.onlinelibrary.wiley.com/doi/abs/10.1002/2016JA023289

Fennell, J. F., Koons, H. C., Roeder, J. L., & Blake, J. B. (2001). Spacecraft charging: Observations and relationship to satellite anomalies. In R. A. Harris (Ed.), Spacecraft charging technology. (Vol. 476, pp. 279).

Fok, M.-C., Buzulukova, N. Y., Chen, S.-H., Glocer, A., Nagai, T., Valek, P., et al. (2014). The comprehensive inner magnetosphere-ionosphere model. *Journal of Geophysical Research: Space Physics*, *119*, 7522–7540. https://doi.org/10.1002/2014JA020239

Fok, M.-C., Glocer, A., Zheng, Q., Horne, R. B., Meredith, N. P., Albert, J. M., et al. (2011). Recent developments in the radiation belt environment model. *Journal of Atmospheric and Solar-Terrestrial Physics*, *73*, 1435–1443. https://doi.org/10.1016/j.jastp.2010.09.033

Fok, M.-C., Horne, R. B., Meredith, N. P., & Glauert, S. A. (2008). Radiation Belt Environment model: Application to space weather nowcasting. *Journal of Geophysical Research*, *113*, A03S08. https://doi.org/10.1029/2007JA012558

Foster, J. C., Erickson, P. J., Baker, D. N., Claudepierre, S. G., Kletzing, C. A., Kurth, W., et al. (2014). Prompt energization of relativistic and highly relativistic electrons during a substorm interval: Van Allen Probes observations. *Geophysical Research Letters*, *41*, 20–25. https://doi.org/10.1002/2013GL058438

Glauert, S. A., Horne, R. B., & Meredith, N. P. (2014). Three-dimensional electron radiation belt simulations using the BAS Radiation Belt Model with new diffusion models for chorus, plasmaspheric hiss, and lightning-generated whistlers. *Journal of Geophysical Research: Space Physics*, *119*, 268–289. https://doi.org/10.1002/2013JA019281

Hayakawa, M., Ohmi, N., Parrot, M., & Lefeuvre, F. (1986). Direction finding of ELF hiss emissions in a detached plasma region of the magnetosphere. *Journal of Geophysical Research*, *91*, 135–142. https://doi.org/10.1029/JA091iA01p00135

Horne, R. B., & Thorne, R. M. (1998). Potential waves for relativistic electron scattering and stochastic acceleration during magnetic storms. *Geophysical Research Letters*, *25*, 3011–3014. https://doi.org/10.1029/98GL01002

Horne, R. B., & Thorne, R. M. (2003). Relativistic electron acceleration and precipitation during resonant interactions with whistler-mode chorus. *Geophysical Research Letters*, *30*, 1527. https://doi.org/10.1029/2003GL016973

Horne, R. B., Thorne, R. M., Glauert, S. A., Albert, J. M., Meredith, N. P., & Anderson, R. R. (2005a). Timescale for radiation belt electron acceleration by whistler mode chorus waves. *Journal of Geophysical Research*, *110*(A3), A03225. http://dx.doi.org/10.1029/2004JA010811

Horne, R. B., Thorne, R. M., Shprits, Y. Y., Meredith, N. P., Glauert, S. A., Smith, A. J., et al. (2005b). Wave acceleration of electrons in the Van Allen radiation belts. *Nature*, *437*(227), 227–230.

Jaynes, A. N., Baker, D. N., Singer, H. J., Rodriguez, J. V., Loto'aniu, T. M., Ali, A. F., et al. (2015). Source and seed populations for relativistic electrons: Their roles in radiation belt changes. *Journal of Geophysical Research: Space Physics*, *120*, 7240–7254. https://doi.org/10.1002/2015JA021234

Kanekal, S. G., Baker, D. N., Henderson, M. G., Li, W., Fennell, J. F., Zheng, Y., et al. (2015). Relativistic electron response to the combined magnetospheric impact of a coronal mass ejection overlapping with a high-speed stream: Van Allen Probes observations. *Journal of Geophysical Research: Space Physics*, *120*, 7629–7641. https://doi.org/10.1002/2015JA021395

Kennel, C. F., & Petschek, H. E. (1966). Limit on stably trapped particle fluxes. *Journal of Geophysical Research*, *71*, 1.

Kim, K.-C., Lee, D.-Y., & Shprits, Y. (2015). Dependence of plasmaspheric hiss on solar wind parameters and geomagnetic activity and modeling of its global distribution. *Journal of Geophysical Research: Space Physics*, *120*, 1153–1167. https://doi.org/10.1002/2014JA020687

Kletzing, C. A., Kurth, W. S., Acuna, M., MacDowall, R. J., Torbert, R. B., Averkamp, T., et al. (2013). The Electric and Magnetic Field Instrument Suite and Integrated Science (EMFISIS) on RBSP. *Space Science Reviews*, *179*, 127–181. https://doi.org/10.1007/s11214-013-9993-6

Kurth, W. S., De Pascuale, S., Faden, J. B., Kletzing, C. A., Hospodarsky, G. B., Thaller, S., et al. (2015). Electron densities inferred from plasma wave spectra obtained by the Waves instrument on Van Allen Probes. *Journal of Geophysical Research: Space Physics*, *120*, 904–914. https://doi.org/10.1002/2014JA020857

Larsen, B., Klumpar, D., & Gurgiolo, C. (2007). Correlation between plasmapause position and solar wind parameters. *Journal of Atmospheric and Solar-Terrestrial Physics*, *69*(3), 334–340. http://dx.doi.org/10.1016/j.jastp.2006.06.017

Lauben, D. S., Inan, U. S., Bell, T. F., & Gurnett, D. A. (2002). Source characteristics of ELF/VLF chorus. *Journal of Geophysical Research*, *107*, 1429. https://doi.org/10.1029/2000JA003019

LeDocq, M. J., Gurnett, D. A., & Hospodarsky, G. B. (1998). Chorus Source Locations from VLF Poynting flux measurements with the Polar spacecraft. *Geophysical Research Letters*, *25*, 4063. https://doi.org/10.1029/1998GL900071

Li, W., Bortnik, J., Thorne, R. M., & Angelopoulos, V. (2011). Global distribution of wave amplitudes and wave normal angles of chorus waves using THEMIS wave observations. *Journal of Geophysical Research*, *116*(A15), 12205. https://doi.org/10.1029/2011JA017035

Li, X. F., & Cho, H.-R. (1997). Development and propagation of equatorial waves. *Advances in Atmospheric Sciences*, *14*, 323–338. https://doi.org/10.1007/s00376-997-0053-6

Li, W., Ni, B., Thorne, R. M., Bortnik, J., Green, J. C., Kletzing, C. A., et al. (2013). Constructing the global distribution of chorus wave intensity using measurements of electrons by the POES satellites and waves by the Van Allen Probes. *Geophysical Research Letters*, *40*, 4526–4532. https://doi.org/10.1002/grl.50920

Li, W., Thorne, R. M., Angelopoulos, V., Bortnik, J., Cully, C. M., Ni, B., et al. (2009). Global distribution of whistler-mode chorus waves observed on the THEMIS spacecraft. *Geophysical Research Letters*, *36*, 9104. https://doi.org/10.1029/2009GL037595

Li, W., Thorne, R. M., Bortnik, J., Nishimura, Y., Angelopoulos, V., Chen, L., et al. (2010). Global distributions of suprathermal electrons observed on THEMIS and potential mechanisms for access into the plasmasphere. *Journal of Geophysical Research*, *115*, A00J10. https://doi.org/10.1029/2010JA015687

Li, W., Thorne, R. M., Ma, Q., Ni, B., Bortnik, J., Baker, D. N., et al. (2014). Radiation belt electron acceleration by chorus waves during the 17 March 2013 storm. *Journal of Geophysical Research: Space Physics*, *119*, 4681–4693. https://doi.org/10.1002/2014JA019945

Lyons, L. R., & Thorne, R. M. (1973). Equilibrium structure of radiation belt electrons. *Journal of Geophysical Research*, *78*, 2142–2149. https://doi.org/10.1029/JA078i013p02142

Lyons, L. R., Thorne, R. M., & Kennel, C. F. (1972). Pitch-angle diffusion of radiation belt electrons within the plasmasphere. *Journal of Geophysical Research*, *77*, 3455. https://doi.org/10.1029/JA077i019p03455

Malaspina, D. M., Jaynes, A. N., Boulé, C., Bortnik, J., Thaller, S. A., Ergun, R. E., et al. (2016). The distribution of plasmaspheric hiss wave power with respect to plasmapause location. *Geophysical Research Letters*, *43*, 7878–7886. https://doi.org/10.1002/2016GL069982

Mauk, B. H., Fox, N. J., Kanekal, S. G., Kessel, R. L., Sibeck, D. G., & Ukhorskiy, A. (2013). Science Objectives and Rationale for the Radiation Belt Storm Probes Mission. *Space Science Reviews*, *179*, 3–27. https://doi.org/10.1007/s11214-012-9908-y

McPherron, R. L., Hsu, T.-S., & Chu, X. (2015). An optimum solar wind coupling function for the al index. *Journal of Geophysical Research: Space Physics*, *120*(4), 2494–2515. https://doi.org/10.1002/2014JA020619

Meredith, N. P., Cain, M., Horne, R. B., Thorne, R. M., Summers, D., & Anderson, R. R. (2003). Evidence for chorus-driven electron acceleration to relativistic energies from a survey of geomagnetically disturbed periods. *Journal of Geophysical Research: Space Physics*, *108*(A6), 967–969. https://doi.org/10.1029/2002JA009764

Meredith, N. P., Horne, R. B., & Anderson, R. R. (2001). Substorm dependence of chorus amplitudes: Implications for the acceleration of electrons to relativistic energies. *Journal of Geophysical Research*, *106*, 13165–13178. https://doi.org/10.1029/2000JA900156

Meredith, N. P., Horne, R. B., Bortnik, J., Thorne, R. M., Chen, L., Li, W., et al. (2013). Global statistical evidence for chorus as the embryonic source of plasmaspheric hiss. *Geophysical Research Letters*, *40*, 2891–2896. https://doi.org/10.1002/grl.50593

Meredith, N. P., Horne, R. B., Glauert, S. A., & Anderson, R. R. (2007). Slot region electron loss timescales due to plasmaspheric hiss and lightning-generated whistlers. *Journal of Geophysical Research*, *112*, A08214. https://doi.org/10.1029/2007JA012413

Meredith, N. P., Horne, R. B., Glauert, S. A., Thorne, R. M., Summers, D., Albert, J. M., et al. (2006). Energetic outer zone electron loss timescales during low geomagnetic activity. *Journal of Geophysical Research*, *111*(A05212). https://doi.org/10.1029/2005JA011516

Meredith, N. P., Horne, R. B., Kersten, T., Li, W., Bortnik, J., Sicard, A., et al. (2018). Global model of plasmaspheric hiss from multiple satellite observations. *Journal of Geophysical Research: Space Physics*, *123*(6), 4526–4541. https://doi.org/10.1029/2018JA025226

Meredith, N. P., Horne, R. B., Shen, X.-C., Li, W., & Bortnik, J. (2020). Global model of whistler mode chorus in the near-equatorial region (—m—¡ 18°). *Geophysical Research Letters*, *47*(11) e2020GL087311. https://doi.org/10.1029/2020GL087311

Meredith, N. P., Horne, R. B., Sicard-Piet, A., Boscher, D., Yearby, K. H., Li, W., et al. (2012). Global model of lower band and upper band chorus from multiple satellite observations. *Journal of Geophysical Research*, *117*(A16), 10225. https://doi.org/10.1029/2012JA017978

Meredith, N. P., Horne, R. B., Thorne, R. M., & Anderson, R. R. (2003). Favored regions for chorus-driven electron acceleration to relativistic energies in the Earth's outer radiation belt. *Geophysical Research Letters*, *30*, 1871. https://doi.org/10.1029/2003GL017698

Meredith, N. P., Horne, R. B., Thorne, R. M., Summers, D., & Anderson, R. R. (2004). Substorm dependence of plasmaspheric hiss. *Journal of Geophysical Research*, *109*, 6209. https://doi.org/10.1029/2004JA010387

Nishimura, Y., Bortnik, J., Li, W., Thorne, R. M., Chen, L., Lyons, L. R., et al. (2011). Multievent study of the correlation between pulsating aurora and whistler mode chorus emissions. *Journal of Geophysical Research*, *116*(A15), A11221. https://doi.org/10.1029/2011JA016876

Nishimura, Y., Bortnik, J., Li, W., Thorne, R. M., Lyons, L. R., Angelopoulos, V., et al. (2010). Identifying the driver of pulsating aurora. *Science*, *330*, 81. https://doi.org/10.1126/science.1193186

Ni, B., Thorne, R. M., Shprits, Y. Y., & Bortnik, J. (2008). Resonant scattering of plasma sheet electrons by whistler-mode chorus: Contribution to diffuse auroral precipitation. *Geophysical Research Letters*, *35*, 11106. https://doi.org/10.1029/2008GL034032

Obara, T., Den, M., Miyoshi, Y., & Morioka, A. (2000). Energetic electron variation in the outer radiation zone during early May 1998 magnetic storm. *Journal of Atmospheric and Solar-Terrestrial Physics*, *62*, 1405–1412. https://doi.org/10.1016/S1364-6826(00)00154-1

Parrot, M., & Lefeuvre, F. (1986). Statistical study of the propagation characteristics of ELF hiss observed on GEOS-1, inside and outside the plasmasphere. *Annales Geophysicae*, *4*, 363–383.

Reeves, G. D., McAdams, K. L., Friedel, R. H. W., & O'Brien, T. P. (2003). Acceleration and loss of relativistic electrons during geomagnetic storms. *Geophysical Research Letters*, *30*, 1529. https://doi.org/10.1029/2002GL016513

Reeves, G. D., Morley, S., & Cunningham, G. (2013). Long-term variations in solar wind velocity and radiation belt electrons. *Journal of Geophysical Research: Space Physics*, *118*, 1040–1048. https://doi.org/10.1002/jgra.50126

Santolík, O., & Gurnett, D. A. (2003). Transverse dimensions of chorus in the source region. *Geophysical Research Letters*, *30*, 1031. https://doi.org/10.1029/2002GL016178

Sheeley, B. W., Moldwin, M. B., Rassoul, H. K., & Anderson, R. R. (2001). An empirical plasmasphere and trough density model: CRRES observations. *Journal of Geophysical Research*, *106*, 25631–25642. https://doi.org/10.1029/2000JA000286

Shprits, Y. Y., Subbotin, D., & Ni, B. (2009). Evolution of electron fluxes in the outer radiation belt computed with the VERB code. *Journal of Geophysical Research: Space Physics*, *114*(A13), 11209. https://doi.org/10.1029/2008JA013784

Subbotin, D. A., & Shprits, Y. Y. (2009). Three-dimensional modeling of the radiation belts using the Versatile Electron Radiation Belt (VERB) code. *Space Weather*, *7*, S10001. https://doi.org/10.1029/2008SW000452

Summers, D., Ma, C., Meredith, N. P., Horne, R. B., Thorne, R. M., Heynderickx, D., et al. (2002). Model of the energization of outer-zone electrons by whistler-mode chorus during the October 9, 1990 geomagnetic storm. *Geophysical Research Letters*, *29*(24), 2174. http://dx.doi.org/10.1029/2002GL016039

Summers, D., Ni, B., & Meredith, N. P. (2007). Timescales for radiation belt electron acceleration and loss due to resonant wave-particle interactions: 2. Evaluation for VLF chorus, ELF hiss, and electromagnetic ion cyclotron waves. *Journal of Geophysical Research*, *112*, 4207. https://doi.org/10.1029/2006JA011993

Summers, D., Thorne, R. M., & Xiao, F. (1998). Relativistic theory of wave-particle resonant diffusion with application to electron acceleration in the magnetosphere. *Journal of Geophysical Research*, *103*, 20487–20500. https://doi.org/10.1029/98JA01740

Thorne, R. M. (2010). Radiation belt dynamics: The importance of wave-particle interactions. *Geophysical Research Letters*, *37*, 22107. https://doi.org/10.1029/2010GL044990

Thorne, R. M., Li, W., Ni, B., Ma, Q., Bortnik, J., Chen, L., et al. (2013). Rapid local acceleration of relativistic radiation-belt electrons by magnetospheric chorus. *Nature*, *504*, 411–414. https://doi.org/10.1038/nature12889

Thorne, R. M., O'Brien, T. P., Shprits, Y. Y., Summers, D., & Horne, R. B. (2005). Timescale for MeV electron microburst loss during geomagnetic storms. *Journal of Geophysical Research*, *110*, 9202. https://doi.org/10.1029/2004JA010882

Thorne, R. M., Smith, E. J., Burton, R. K., & Holzer, R. E. (1973). Plasmaspheric hiss. *Journal of Geophysical Research*, *78*, 1581–1596. https://doi.org/10.1029/JA078i010p01581

Tsurutani, B. T., Falkowski, B. J., Pickett, J. S., Santolik, O., & Lakhina, G. S. (2015). Plasmaspheric hiss properties: Observations from polar. *Journal of Geophysical Research: Space Physics*, *120*(1), 414–431. https://agupubs.onlinelibrary.wiley.com/doi/abs/10.1002/2014JA020518

Tsurutani, B. T., Park, S. A., Falkowski, B. J., Lakhina, G. S., Pickett, J. S., Bortnik, J., et al. (2018). Plasmaspheric hiss: Coherent and intense. *Journal of Geophysical Research: Space Physics*, *123*(12), 10009–10029. https://agupubs.onlinelibrary.wiley.com/doi/abs/10.1029/2018JA025975

Tsurutani, B. T., & Smith, E. J. (1974). Postmidnight chorus: A substorm phenomenon. *Journal of Geophysical Research*, *79*, 118–127. https://doi.org/10.1029/JA079i001p00118

Tu, W., Cunningham, G. S., Chen, Y., Morley, S. K., Reeves, G. D., Blake, J. B., et al. (2014). Event-specific chorus wave and electron seed population models in DREAM3D using the Van Allen Probes. *Geophysical Research Letters*, *41*, 1359–1366. https://doi.org/10.1002/2013GL058819

Van Allen, J. A. (1959). The geomagnetically trapped corpuscular radiation. *Journal of Geophysical Research*, *64*, 1683–1689. https://doi.org/10.1029/JZ064i011p01683

Wygant, J. R., Bonnell, J. W., Goetz, K., Ergun, R. E., Mozer, F. S., Bale, S. D., et al. (2013). The electric field and waves instruments on the radiation belt storm probes mission. *Space Science Reviews*, *179*, 183–220. https://doi.org/10.1007/s11214-013-0013-7

Xiao, F., Su, Z., Zheng, H., & Wang, S. (2010). Three-dimensional simulations of outer radiation belt electron dynamics including cross-diffusion terms. *Journal of Geophysical Research*, *115*, A05216. https://doi.org/10.1029/2009JA014541